Title

Effect of Fluorination on Lithium Transport and Short-Range Order in Disordered-Rocksalt-Type Lithium-Ion Battery Cathodes

Journal

Advanced Energy Materials, 10(10)

ISSN

1614-6832

Authors

Ouyang, Bin
Artrith, Nongnuch
Lun, Zhengyan
et al.

Publication Date

2020-03-01

DOI

10.1002/aenm.201903240

Peer reviewed

Effect of Fluorination on Lithium Transport in Rock-Salt-Type Lithium-Ion Battery Cathodes

Nongnuch Artrith,[1,2,a)] Zhengyan Lun,[1,2] Zinab Jadidi,[1,2] Alexander Urban,[3] and Gerbrand Ceder[1,2,b)]

[1)] *Department of Materials Science and Engineering, University of California, Berkeley, CA, USA*

[2)] *Materials Science Division, Lawrence Berkeley National Laboratory, Berkeley, CA, USA*

[3)] *School of Chemistry, University of St Andrews, UK*

(Dated: 2018-11-27)

Abstract

Cation-disordered rock-salt (DRX) materials are a new class of high-capacity Li-ion battery cathode materials in which Li diffusion can occur despite cation mixing. Li transport in DRX materials relies on low-barrier diffusion channels that only become percolating in Li-rich compositions. In the limit of fully stochastic cation disorder, at least 10% Li excess is needed for percolation to occur. It has recently been demonstrated that fluorine substitution of some of the lattice oxygen in DRX materials is possible because of the strong attractive interactions between Li and F atoms. In this work, we investigated how this Li−F attraction affects the Li transport and percolation limits in fluorinated DRX materials. We constructed a simple lattice model that captures the essential Li−F interactions and is otherwise agnostic with respect to the composition. Using Monte-Carlo simulations coupled with percolation analysis, we determined that fluorine substitution is beneficial for Li transport in DRX materials. The Li content in oxyfluorides can be significantly reduced compared with that in non-fluorinated oxides without affecting the high capacity of the materials, and even compositions with only 5% excess Li can exhibit high capacities. We confirmed this computational prediction by experimental comparison of the fluorinated $Li_{1.05}Ni_{0.533}Ti_{0.373}Mo_{0.033}O_{1.85}F_{0.15}$ with its unfluorinated counterpart $Li_{1.05}Ni_{0.458}Ti_{0.458}Mo_{0.033}O_2$, demonstrating that the capacity of the fluorinated composition was nearly 40% greater.

[a)]Electronic mail: nartrith@atomistic.net

[b)]Electronic mail: gceder@berkeley.edu

I. INTRODUCTION

Rock-salt-type lithium transition-metal (TM) oxides have recently emerged as a new class of high-capacity cathodes for Li-ion batteries (LIBs).[1–11] In contrast to conventional layered or spinel-type cathodes, Li and TM ions occupy equivalent lattice sites in cation-disordered rock-salt (DRX) cathodes. Li transport in DRX materials is enabled by fast Li-rich diffusion channels that become percolating in Li-excess compositions.[1,12]

One advantage of DRX materials compared with conventional layered or spinel-type Li-TM oxides is the feasibility of fluorine substitution of some of the lattice oxygen. Fluorination of layered cathode materials typically leads to either segregation of a LiF phase or cation mixing and the eventual loss of order,[13–16] which negatively affect the capacity. Fluorination of spinel materials is possible in some cases with the ordered structure maintained and has been reported to have a beneficial effect on the capacity retention.[17,18] Fluorination of DRX materials, however, appears to be generally possible and highly beneficial. Fluorine substitution can significantly improve the stability of DRX materials against decomposition by irreversible oxygen loss[19,20] and enables the achievement of remarkable capacities and energy densities.[4,11,21–25]

Motivated by these recent discoveries of high-capacity oxyfluorides, we investigate here how fluorination affects Li transport and the practical capacity in DRX materials. Li transport in DRX structures is mechanistically complex and highly dependent on the composition. In DRX cathodes, Li transport occurs through fast *0-TM* Li diffusion channels that are only present in sufficient concentration in compositions containing at least around 10% Li excess, and even higher Li contents ($\sim 20\%$) are required to achieve high capacities of up to 1 Li atom per $Li_{1+x}M_{1-x}O_2$ (M = other metal cation species) formula unit.[12] In addition, short-range order (SRO) can further alter the Li transport and thereby change the optimal Li content.[26]

Computational studies using lattice model simulations[27,28] and experimental solid-state nuclear magnetic resonance (NMR) measurements[28] have established that F substitution does not occur homogeneously in the anion sublattice in DRX materials. Instead, F strongly prefers Li-rich environments in which LiF-like domains are formed, and M–F bonds have been predicted to be unfavorable by computation.[27,28] As a consequence of this bonding preference, fluorinated materials exhibit strong SRO on the atomic scale despite their apparent disorder

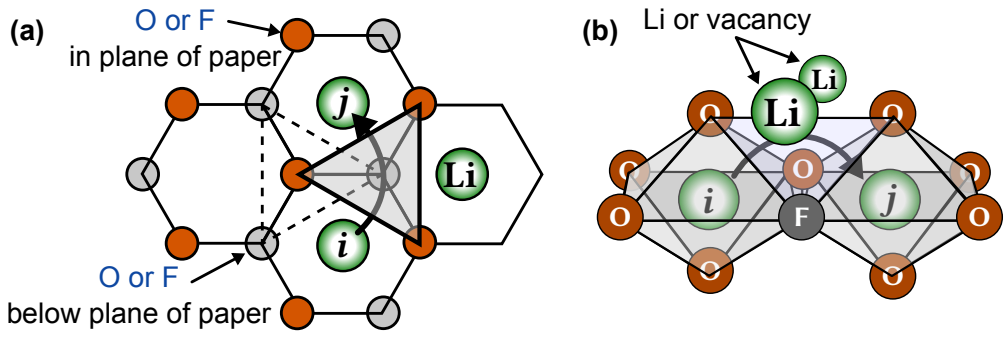

FIG. 1. **0-TM diffusion channel and o-t-o mechanism.** The hop from one octahedral Li site i to another octahedral site j via a tetrahedral intermediate state as seen **(a)** along the cubic (111) direction and **(b)** in a perspective visualization. The tetrahedral intermediate of 0-TM channels is only coordinated by Li atoms (or vacancies once the Li sites have been vacated) as shown in panel **(b)**. Fluorination replaces some of the oxygen atoms (red) with fluorine atoms (gray circles in **(b)**), which may affect the activation energy for Li hops.

on the macroscopic scale.

In the present work, our aim was to determine the effect of these strong Li−F interactions and the resulting SRO on the percolation of 0-TM diffusion channels and the Li transport. In the Methods section, we introduce a computational model that incorporates the previously observed[27,28] atomic Li−F interaction tendency in rock-salt-type oxyfluorides into Li transport simulations. We applied this methodology to obtain insight into the effect of F substitution on Li percolation and the expected capacity. Finally, we experimentally validated the computational predictions for cation-disordered $Li_{1.05}(Ni, Ti, Mo)_{0.95}(O, F)_2$.

II. METHODS

A. Li Percolation Theory

In rock-salt-type oxides, including DRX structures and those with the layered α-$NaFeO_2$ crystal structure such as $LiCoO_2$, the cation sites are octahedral. Li transport occurs on the atomic scale as hops between two octahedral sites via a tetrahedral intermediate in the presence of a second Li vacancy.[29,30] This o-t-o divacancy mechanism is schematically illustrated in **Fig. 1**.

In cation-disordered structures, three types of diffusion channels exist that can be classified

as 0-TM, 1-TM, and 2-TM depending on the number of TM ions that coordinate with the intermediate tetrahedral site.[12] In layered materials, cation disorder results in contraction of the c-lattice parameter such that the type of Li diffusion channel that is active in layered materials (1-TM channels) is mostly inactive or slow in disordered phases.[12,31] Because of the electrostatic repulsion between the high-valent metal ion and the diffusing Li^+ ion,[30,31] the activation energy for diffusion through 0-TM channels is on average the lowest ($\sim$ 300 meV)[1]. A lower bound on the capacity can be obtained by considering Li atoms only extractable when they are on cation sites connected to percolating 0-TM pathways.[12]

A 0-TM channel is essentially a tetrahedral interstitial site that connects two octahedral Li sites and is itself only coordinated by Li or vacancy sites and not by other metal cations (**Fig. 1**). As 0-TM channels are locally Li rich, their concentration increases with increasing Li content in the composition. Percolation simulations have shown that an excess Li content of approximately 10% (i.e., $Li_{1+x}M_{1-x}O_2$ with $x \approx 0.1$) is required for 0-TM channels to form percolating diffusion pathways in fully cation-mixed structures.[12] However, even when percolating 0-TM diffusion pathways exist, not all of the Li sites are necessarily connected to the percolating network. Higher Li contents of $\sim$20% Li excess are needed to enable the reversible extraction of approximately 1 Li atom per formula unit, which corresponds to a high capacity (>200 $mAh\,g^{-1}$).[12]

In the present work, we employed the lattice-model percolation simulation methodology that we previously developed for unfluorinated DRX materials.[1,12,32] These percolation simulations are agnostic with respect to the M species and only depend on the definition of the active diffusion channel, i.e., the 0-TM channel, with the advantage that the results of the simulations are transferable across different DRX compositions.

B. Simulating Realistic Short-Range Order (SRO)

It is a common feature of fluorine-substituted Li-TM oxides across different compounds and metal cation (M) species that Li−F bonds are strongly preferred over M−F bonds,[27,28] as detailed above. From the perspective of an interaction energy model, the Li−F interactions are thus net attractive (negative energy contributions), whereas the M−F interactions are net repulsive (positive). The precise magnitude of the energetic difference between Li−F and M−F interactions depends on the M species; however, the trends are general across different

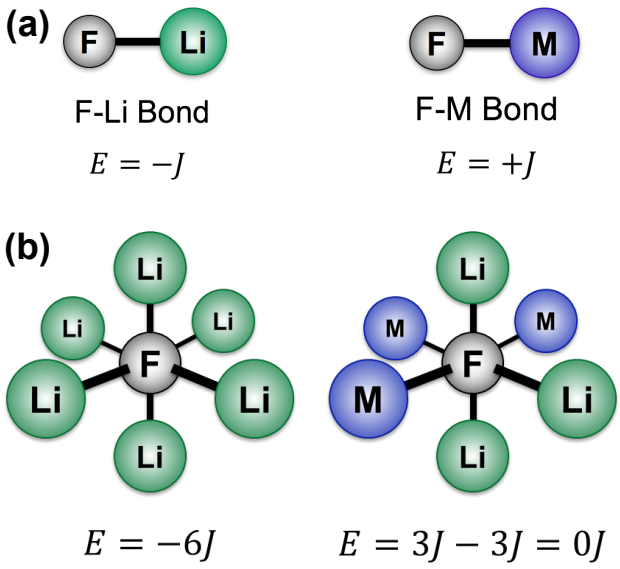

FIG. 2. **Schematic illustrations of bonding and site energies in the employed lattice model. (a)** The bond energies are expressed in terms of a positive effective interaction parameter J and capture the Li−F attraction and M−F repulsion (M = other metal cation species). With this bond energy definition, the energy of each F site lies between $-6J$ and $+6J$. Two examples are shown in panel **(b)**.

compounds. Based on this observation, we constructed a general pairwise interaction model that is, within the scope of our application, transferable to any (transition) metal species.

To simulate realistic SRO in fluorinated DRX, we employed a lattice model of the rock-salt structure comprising two interpenetrating face-centered-cubic sublattices for the cations and anions. Two assumptions underlie our model: First, we only considered SRO arising from fluorination, i.e, SRO that is driven by the Li−F attraction and M−F repulsion. SRO that is present in the unfluorinated oxide and caused by Li−M interactions was disregarded in this model as it is specific to the M species and independent of fluorination. Second, we further assumed that the Li−F and M−F interactions that determine the SRO relevant for the percolation properties are captured by pairwise and short-ranged contributions.

With these two assumptions, the Li−F interaction energy $E_{\text{Li-F}}$ and the (M-species-specific) M−F interaction energy $E_{\text{M-F}}$ are the only physical interactions needed, and a single *effective* interaction parameter

$$J = \frac{E_{\text{M-F}} - E_{\text{Li-F}}}{2} \tag{1}$$

is sufficient to define the lattice model (**Fig. 2a**).

Within this simple model, the energy of an F site i is

$$E_i^{\mathrm{F}} = J \sum_{j=1}^{6} \sigma_j \quad \text{with } \sigma_j = \begin{cases} 1 & \text{if site } j \text{ is a M site} \\ -1 & \text{if site } j \text{ is a Li site} \end{cases} , \tag{2}$$

where the sum runs over the six neighboring cation sites (**Fig. 2b**). The mean energy per F site of a given structure S with a total of N_{F} F atoms is

$$\overline{E}^{\mathrm{F}}(S) = \frac{1}{N_{\mathrm{F}}} \sum_{i}^{\text{F sites}} E_i^{\mathrm{F}} \quad . \tag{3}$$

This lattice model has a number of interesting properties: The ground-state energy $\overline{E}_0^{\mathrm{F}} = -6J$ does not depend on the actual composition or the number of F atoms, though it can only be realized if there is sufficient Li available such that every F site is only coordinated by Li. For a given composition $\mathrm{Li}_x\mathrm{M}_{2-x}\mathrm{O}_{2-y}\mathrm{F}_y$, the energy of a fully random atomic ordering approaches

$$\overline{E}_{\infty}^{\mathrm{F}}(x) = 6(1-x)J, \tag{4}$$

which only depends on the ratio of Li to M in the composition and is exactly 0 for the stoichiometric composition with $x = 1$.

Most importantly, the energy of each atomic configuration can be expressed relative to the effective interaction parameter J such that the physics of the system described by the lattice model does not depend on the actual value of J. Hence, we can set $J = 1$ without loss of generality, and a connection with an actual M species or a mixture of different metal species can be made *a posteriori* by determining the value of J that best describes the specific composition, for example by fitting to first-principles calculations or by comparison of the universal J-dependent phase diagram with an experimental or first-principles phase diagram.

C. Phase Diagram Calculations

Using the above interaction model, structures with realistic SRO were sampled using Monte Carlo (MC) simulations. We employed grand canonical (μVT) Monte Carlo (GCMC) simulations to construct the temperature-dependent phase diagram of the model system, i.e.,

the ranges of x and y in $\mathrm{Li}_x\mathrm{M}_{2-x}\mathrm{O}_{2-y}\mathrm{F}_y$ that belong to compositions that can be realized as solid solutions at a given temperature.[33] The GCMC Hamiltonian is

$$H = \sum_{i}^{\text{F sites}} E_i^{\mathrm{F}} - \mu_{\mathrm{Li}} N_{\mathrm{Li}} - \mu_{\mathrm{F}} N_{\mathrm{F}}, \tag{5}$$

where μ_{Li} and μ_{F} are the chemical potentials of Li and F and N_{Li} and N_{F} are the number of Li and F atoms in the structure, respectively.

Note that the M and O chemical potentials are not present in the Hamiltonian equation (5). The chemical potentials of species that share the same sublattice are interrelated, and only the differences $\mu_{\mathrm{Li}} - \mu_{\mathrm{M}}$ and $\mu_{\mathrm{F}} - \mu_{\mathrm{O}}$ are meaningful. We thus set $\mu_{\mathrm{M}} = \mu_{\mathrm{O}} = 0$ without loss of generality.

Similar to the configuration energy $\overline{E}^{\mathrm{F}}(S)$ of equation (3), the temperature in the GCMC simulations is in units relative to the interaction parameter J ($[T] = J/k_{\mathrm{B}}$, where k_{B} is Boltzmann's constant), and the phase diagram itself is independent of the actual value selected for J. Therefore, once the phase diagram is known for one specific choice of J (such as $J = 1$), the result can be scaled to any other J without repeating the GCMC simulations.

D. Lithium Transport in Fluorinated Phases

After the phase diagram was computed using GCMC simulations, canonical MC simulations were used to sample atomic configurations in the accessible solid-solution composition space. We sampled the composition space of $\mathrm{Li}_x\mathrm{M}_{2-x}\mathrm{O}_{2-y}\mathrm{F}_y$ with $x \in [0.925, 1.500]$ and $y \in [0.0, 0.7]$ for temperatures $T \in [0.1, 6.0]$ J/k_{B}. For each of the sampled compositions and temperatures, 500 configurations with 2,400 lattice sites each were used for further analysis. Further computational details are provided in the appendix.

For each of the generated atomic configurations, it was determined whether the structure was 0-TM percolating (yes/no), and if it was percolating, the number of Li sites connected to percolating 0-TM diffusion pathways was determined. These quantities were averaged over the 500 configurations to obtain a percolation probability and a mean 0-TM connected capacity for every sampled composition. The percolation threshold as a function of the Li content, F content, or temperature was then computed by combining the percolation probabilities from multiple compositions and temperatures.

To confirm that fluorination does not affect the Li diffusion mechanism and that 0-TM

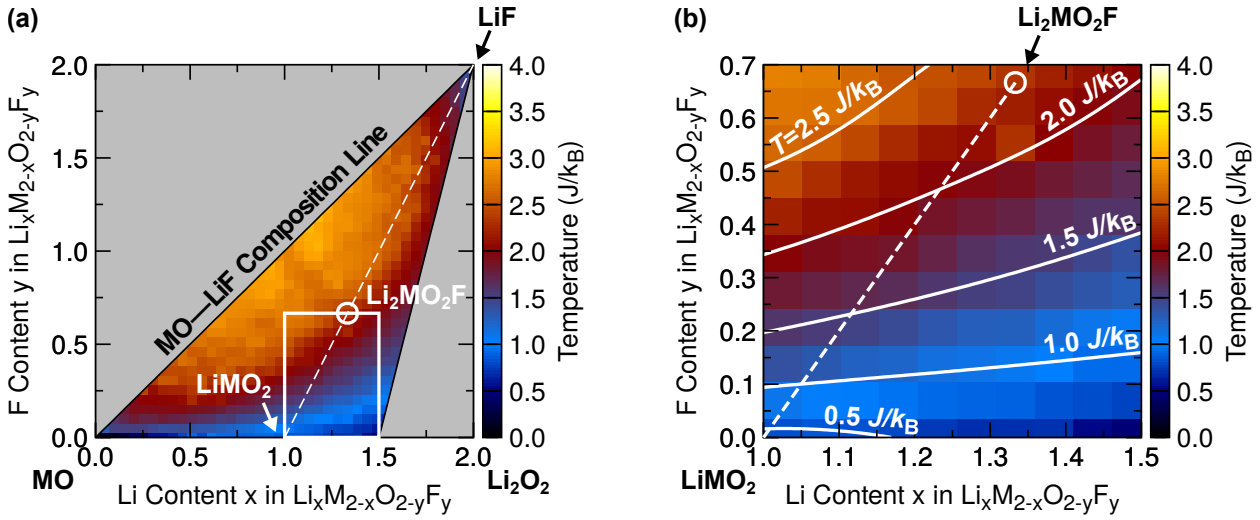

FIG. 3. **Phase diagram from grand-canonical Monte-Carlo simulations.** The color corresponds to the lowest temperature at which each composition $Li_xM_{2-x}O_{2-y}F_y$ occurred in the simulations. **(a)** Phase diagram of the entire composition space. The composition line $LiMO_2$–LiF is indicated by a dashed line. The compositions that are relevant for Li-ion battery cathode materials in practice are enclosed by a white rectangle. **(b)** Magnified version of the region within the rectangle. In both **(a)** and **(b)**, the composition Li_2MO_2F is indicated by a circle.

channels are the active diffusion channels in DRX oxyfluorides, we performed diffusion path simulations for special quasi-random structures (SQS)[34,35] using the climbing-image nudged-elastic-band (NEB) method.[36,37] Representative NEB minimum energy pathways are shown in **Figs. S1 and S2** in the supporting information. As seen in the figures, fluorination only slightly changes the diffusion barriers by less than 0.1 eV. This change is not enough to activate the 1-TM channel or to deactivate the 0-TM channel, and the overall diffusion mechanism therefore remains unchanged.

III. RESULTS

A. Phase Diagram of Fluorinated Rock-Salt Phases

Figure 3 presents the two-dimensional phase diagram of the $Li_xM_{2-x}O_{2-y}F_y$ oxyfluoride composition space obtained from GCMC simulations using the energy model introduced in the Methods section. The figure shows the lowest temperature at which each composition

was observed in the simulations to obtain an approximation of the coexistence (binodal) plane. At low temperatures (shades of blue), phase separation into the end members is favored, whereas more of the composition space can be accessed at higher temperatures (red to yellow regions).

The lattice model is intended for oxyfluoride compositions derived from $LiMO_2$; the phase diagram is thus only meaningful for the region in which realistic oxyfluoride compositions are located. Therefore, only the relevant Gibbs triangle with compositions within the space defined by MO, LiF, and $Li_{1.5}M_{0.5}O_2$ is shown. A more conventional visualization of the phase diagram as an equilateral triangle is provided in supporting **Fig. S3**.

The region of the phase diagram that is most relevant for LIB cathode materials is enclosed by a white rectangle in **Fig. 3a**. This region, shown magnified in **Fig. 3b**, contains compositions with up to 50% Li excess (highly Li-rich compositions) and up to a fluorine content of 33%, which corresponds to the composition Li_2MO_2F. Note that Li_2VO_2F and other oxyfluorides with analogous compositions of other transition metal species can be prepared by mechanochemical synthesis but not via thermal routes[4]; thus, we can deduce that temperatures above $\sim 2.0\ J/k_B$ (colored in shades of red in **Fig. 3**) are usually not accessible using thermal solid-state synthesis.

Note that all compositions that lie directly on the composition line between MO and Li_2O_2 are equivalent for the lattice model as they do not contain any fluorine, and hence, neither Li–F nor M–F interactions are present. However, fluorination of the compositions becomes more facile with increasing Li content (indicated by the growing blue region in the phase diagram) and more difficult when approaching the MO composition because of the attractive Li–F and repulsive M–F interactions.

Previous computational work by Richards et al. using first-principles-based lattice models established that the solubility of fluorine in Li-TM oxides is low and that wide miscibility gaps between the end members $LiMO_2$ and LiF exist even at typical solid-state synthesis temperatures (∼1,000°C).[38] To replicate the properties of a realistic Li-TM oxyfluoride and to allow correlation of the scaled temperature in units of J/k_B with those expected for an actual oxyfluoride composition, our model should show the same qualitative behavior.

Figure 4 shows the one-dimensional phase diagrams along the two composition lines $LiMO_2$–LiF (the line studied by Richards et al.) and MO–LiF, and both show clear miscibility gaps up to temperatures of approximately 2.5 J/k_B and 3.0 J/k_B, respectively. Thus, the

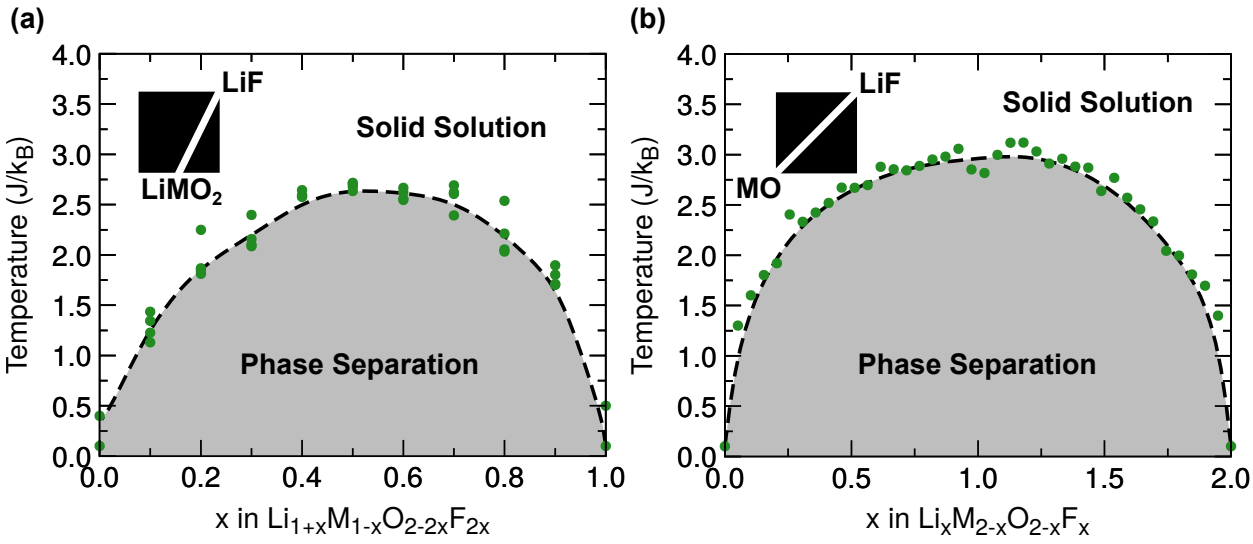

FIG. 4. **Phase diagram along two composition lines.** The one-dimensional phase diagrams correspond to the composition lines between **(a)** $LiMO_2$ and LiF and **(b)** MO and LiF that are also indicated in the two-dimensional phase diagram of Fig. 3. Both phase diagrams show large two-phase regions (gray) in which phase separation into the end members occurs. The data points from Monte Carlo simulations are shown as green dots. The black dashed lines are meant to guide the eye.

simplified general Hamiltonian of equation (5) reproduces the phase-separating behavior seen in real oxyfluorides. At low temperatures, LiF does not mix with $LiMO_2$ and only a small solubility region is thermally accessible. Introducing fluorine becomes more facile with increasing Li content and increasing temperature.

B. Li Transport Properties in Fluorinated Phases

Using the canonical MC protocol outlined in the Methods section, we determined the 0-TM accessible Li content in fluorinated rock-salt structures with realistic SRO. Taken together with the phase diagram of **Fig. 3**, the 0-TM capacity can be analyzed as a function of the Li and/or F content and the temperature. In particular, we can now determine the effect of a specific amount of fluorine substitution on the Li transport properties. A fluorine content of approximately 7.5% was previously observed to enable good capacity retention in DRX cathode materials.[19] We therefore considered 7.5% fluorine substitution, i.e., the general composition $Li_xM_{2-x}O_{1.85}F_{0.15}$, as an example.

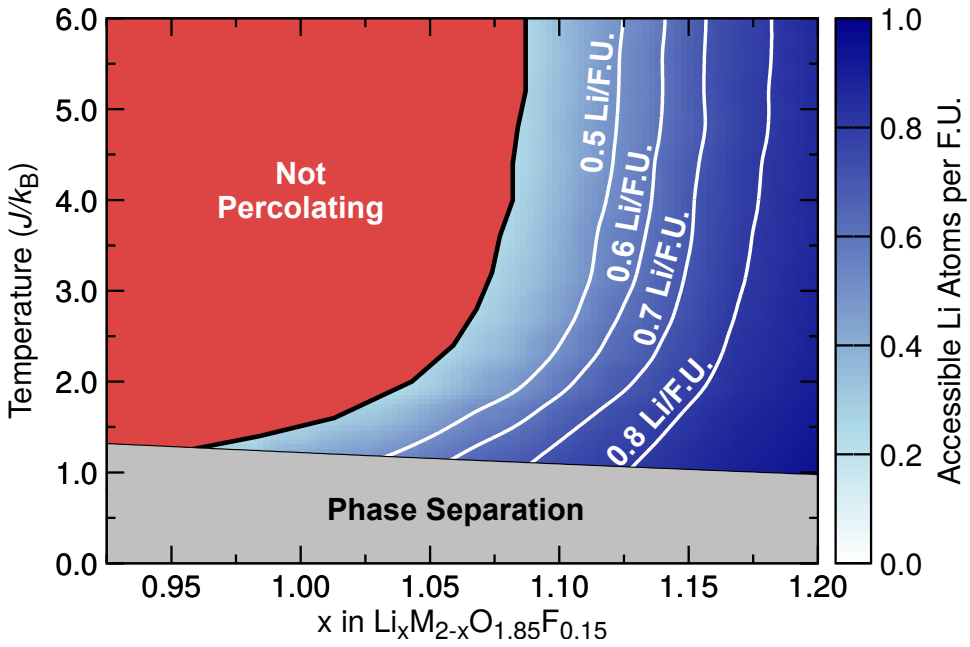

FIG. 5. **0-TM connected capacity for 7.5% fluorination.** The 0-TM connected capacity for compositions $Li_xM_{2-x}O_{1.85}F_{0.15}$ (= 7.5% F substitution) is shown in terms of extractable Li atoms per formula unit (F.U.). The thick black line represents the percolation threshold, and the compositions within the red region are not 0-TM percolating. The gray region at the bottom of the graph is not accessible under equilibrium conditions as it is part of the miscibility gap of the phase diagram in Fig. 3.

Figure 5 shows the temperature-dependent 0-TM percolation threshold and accessible capacity for compositions with 7.5% fluorine substitution. Note that the temperature in the percolation map should be understood as the synthesis temperature and not the operation temperature, and as reasoned in the previous section, temperatures above $T = 2.0\ J/k_B$ are likely not accessible. In addition, at low temperatures, 7.5% of fluorination is not achievable as this value falls in the phase-separation region in the phase diagram (gray region in the percolation map in **Fig. 5**).

From the percolation map, it is immediately obvious that fluorine substitution can have a strong effect on the percolation properties. For very high temperatures approaching 6 J/k_B, the Li−F and M−F interactions are overcome and the atomic ordering becomes essentially random. Therefore, the percolation threshold (indicated by the thick black line in **Fig. 5**) approaches the value for fully disordered unfluorinated rock-salt materials of $x_c \approx 1.09$.[12]

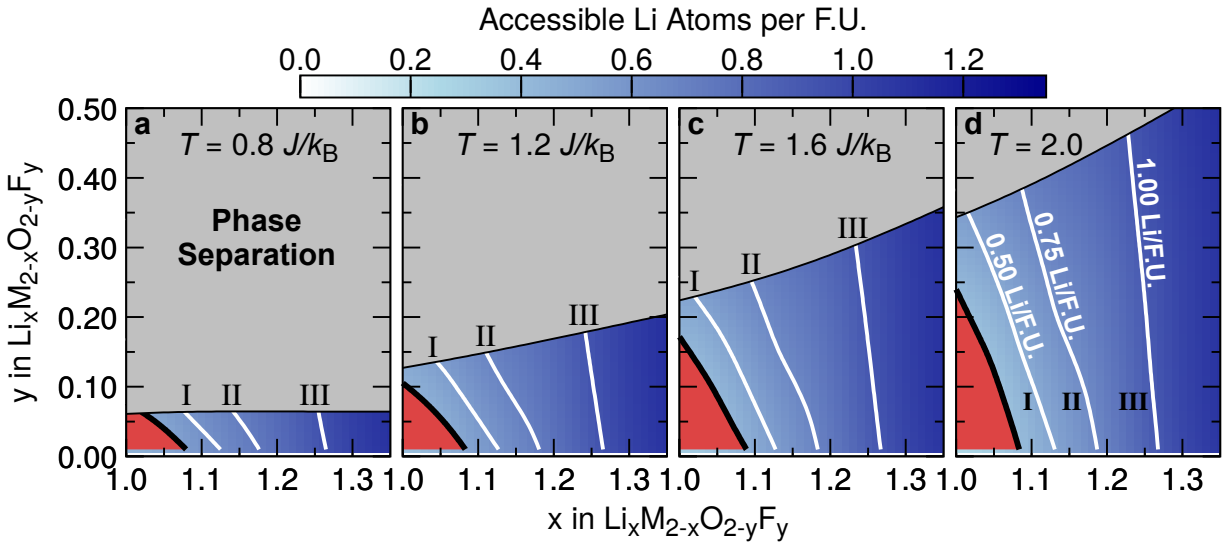

FIG. 6. **Percolation maps as a function of Li and F content.** Accessible compositions and 0-TM capacities at temperatures **(a)** $T = 0.8\ J/k_{\mathrm{B}}$, **(b)** $T = 1.2\ J/k_{\mathrm{B}}$, **(c)** $T = 1.6\ J/k_{\mathrm{B}}$, and **(d)** $T = 2.0\ J/k_{\mathrm{B}}$. With increasing temperature, more compositions become accessible in the phase diagram. The percolation threshold is indicated by a thick black line, and in each panel, three contour lines for the 0-TM connected capacities (I) 0.50 Li/F.U., (II) 0.75 Li/F.U., and (III) 1.00 Li/F.U. are shown. Compositions within the red regions are not percolating, and the gray regions are within the miscibility gap of the phase diagram (see also **Fig. 3**).

However, interestingly, the percolation threshold decreases significantly at lower temperatures, where the SRO is governed by the Li–F and Li–M interactions. Below $T = 1.5\ J/k_{\mathrm{B}}$, the percolation threshold becomes as low as $x_c \approx 0.96$, i.e., no excess Li is required for percolation.

The same trend is also reflected by the amount of 0-TM accessible Li atoms per formula unit (F.U.) that determines the practical capacity of the cathode materials. This 0-TM connected capacity is shown as shades of blue (and white contour lines) in **Fig. 5**. As seen from the contour lines, for example, at a Li content of $x = 1.05$, nearly 0.6 Li/F.U. become accessible under ideal conditions, whereas 5% Li excess is still well below the percolation limit in unfluorinated rock-salt materials.

Instead of considering a specific amount of fluorine substitution, we can alternatively construct percolation maps for select temperatures. **Figure 6** shows the percolation threshold and 0-TM connected capacity as a function of the Li and F content for four different scaled temperatures, again taking $T = 2.0\ J/k_{\mathrm{B}}$ as the thermally accessible limit. With increasing

temperature, higher fluorine contents become accessible such that the area of the miscibility gap (gray region in the percolation maps) decreases from $T = 0.8\ J/k_{\mathrm{B}}$ (panel **a**) to $T = 2.0\ J/k_{\mathrm{B}}$ (panel **d**). The percolation threshold is again shown as a thick black line, and the shades of blue indicate the 0-TM connected capacity. Three selected capacities (I: 0.50, II: 0.75, and III: 1.00 Li per formula unit) are indicated by white contour lines.

In all the percolation maps in **Fig. 6a-d**, the fluorine content of $y = 0$ corresponds to the fully disordered unfluorinated $\mathrm{Li}_x\mathrm{M}_{2-x}\mathrm{O}_2$ oxides, and the percolation threshold and 0-TM capacities of reference 12 are recovered.

Irrespective of the temperature, it is clear from **Fig. 6** that the percolation threshold decreases faster than linearly with the F content. In fact, for all except the lowest temperature ($0.8\ J/k_{\mathrm{B}}$), materials fluorinated up to the solubility limit can achieve 0-TM percolation even without Li excess. Fluorination also generally improves the 0-TM capacity. For example, the amount of Li excess that is needed to extract 0.5 Li/F.U. is reduced from approximately 13% for the unfluorinated case to approximately 5% at the maximal obtainable fluorine content at any of the temperatures. As also seen in the figure, the beneficial effect of fluorination is largest for compositions with low Li content and decreases as the Li excess rises to 25% ($x = 1.25$).

Another insight from **Fig. 6** is that although the temperature determines the feasible degree of fluorination, the 0-TM connected capacities of the compositions with the highest achievable fluorine content for any given Li content are similar across all temperatures. This observation is important as it allows us to estimate the limit of the achievable 0-TM connected capacity independent of the scaled temperature, which in our simulations depends on the metal species M-specific interaction strength J. In other words, the percolation maps in **Fig. 6** indicate that the maximal achievable 0-TM connected capacity at the F solubility limit will be roughly the same independent of the maximum F solubility of a specific material.

C. Experimental Validation

To put theory into practice, we considered a cation-disordered cathode material for experimental validation of the computed percolation trends. We selected compositions derived from cation-disordered $\mathrm{LiNi}_{0.5}\mathrm{Ti}_{0.5}\mathrm{O}_2$[39] as it has previously been reported that Li excess can be introduced by molybdenum doping[40] and that fluorination is possible using

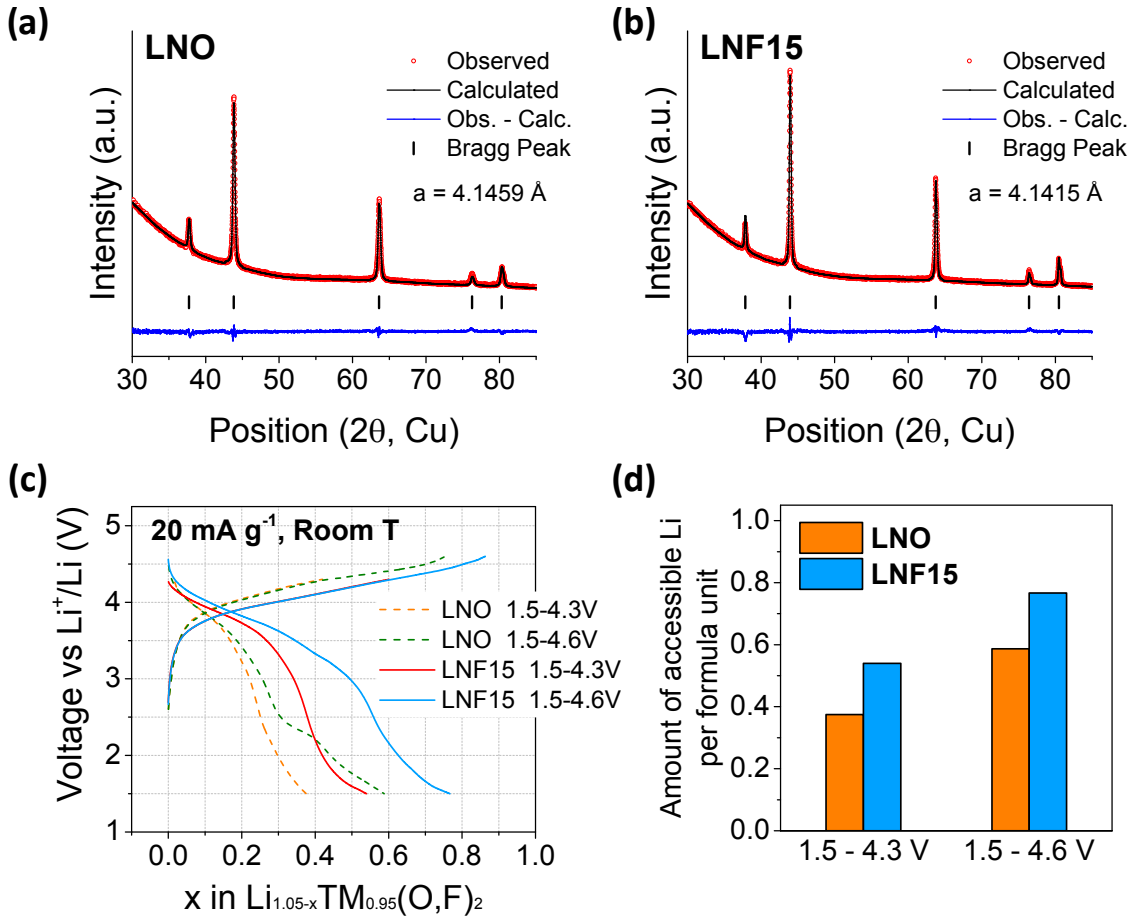

FIG. 7. **Experimental verification of fluorination improving percolation in a cation-disordered rock-salt material.** Powder X-ray diffraction patterns of **(a)** $Li_{1.05}Ni_{0.458}Ti_{0.458}Mo_{0.033}O_2$ (LNO) and **(b)** $Li_{1.05}Ni_{0.533}Ti_{0.373}Mo_{0.033}O_{1.85}F_{0.15}$ (LNF15), which both form as phase-pure rock-salt structures. **(c)** First-cycle charge and discharge voltage profiles of LNO and LNF15 within two different voltage windows of 1.5–4.3 V and 1.5–4.6 V. **(d)** LNO and LNF15 capacity in terms of accessible Li within the two voltage windows as obtained from the voltage profiles in **(c)**.

thermal solid-state synthesis.[19] In principle, these compositions have the additional advantage that both Ni^{2+}/Ni^{3+} and Ni^{3+}/Ni^{4+} redox reactions would be available. However, in previous related unfluorinated materials, oxygen redox participation was observed before all of the Ni^{3+} was fully oxidized.[40] Irrespective of the redox mechanism, the available electron redox is not expected to become capacity limiting.

The percolation analysis shown in **Fig. 5** predicts a 0-TM capacity of 0.5-0.6 Li/F.U. for compositions with only 5% excess Li and a F content of 7.5%, and the percolation maps

in **Fig. 6** indicate that the fluorination has the largest effect on compositions with low Li content. Therefore, we decided to compare two cation-disordered materials with 5% excess Li and (i) no F and (ii) 7.5% fluorination. The target compositions for the two compounds were $Li_{1.05}Ni_{0.458}Ti_{0.458}Mo_{0.033}O_2$ (LNO) and $Li_{1.05}Ni_{0.533}Ti_{0.373}Mo_{0.033}O_{1.85}F_{0.15}$ (LNF15).

Both compounds, LNO and LNF15, were prepared by conventional solid-state synthesis following previously published routes[19,40], as described in the Experimental section. As seen in the X-ray powder diffraction patterns in **Fig. 7a-b**, both materials were phase pure and formed in the disordered rock-salt structure, as expected. Fluorination only resulted in a slight lattice contraction from $a = 4.1459\,\text{Å}$ to $a = 4.1415\,\text{Å}$ as determined from Rietveld refinement.

Before attempting to directly compare the simulation and experimental results, it is important to recall that the 0-TM capacity is a *lower bound* for the actual capacity, as detailed in the Methods section. Even though a Li content of 5% is below the 0-TM percolation threshold of pure oxides, some capacity should be expected for the unfluorinated material owing to contributions from slow migration through 1-TM channels.

Figure 7c presents the first-cycle charge/discharge voltage profiles of the two materials for two different voltage windows. As similar compositions have previously been shown to release oxygen gas during charge,[40] the discharge capacities can be more straightforwardly compared with the predicted 0-TM capacities. In the smaller voltage window (1.5-4.3 V), the unfluorinated LNO delivered a discharge capacity of 0.38 Li/F.U., and in the larger voltage window (1.5-4.6 V), 0.59 Li/F.U. was delivered. Although these capacities are not very high, 5% excess Li is below the 0-TM percolation threshold in fully disordered rock-salt materials, and the observed capacities indicate that the percolation threshold in LNO is either reduced by SRO or that some of the 1-TM channels are active in LNO.

Significantly higher discharge capacities were achieved for the fluorinated LNF15 for both voltage windows. In the smaller voltage window, LNF15 could reversibly cycle 0.52 Li/F.U. (an improvement of 37% over that for LNO), and in the larger voltage window, LNF15 could reversibly cycle 0.78 Li/F.U. (an improvement of 32% over that for LNO). A capacity of 0.8 Li/F.U. is remarkable for a composition with such a small amount of excess Li and is significantly larger than the capacity of commercial rock-salt-type cathodes, which only allow for reversible extraction of ∼0.7 Li at most.[41] This result clearly indicates that fluorination improved the Li percolation of the material.

IV. DISCUSSION

Both the lattice-model simulations and experiment followed by electrochemical characterization indicate that fluorination is beneficial for Li transport in fluorinated rock-salt-type cathodes. In particular, F substitution systematically reduces the amount of Li excess required to achieve high capacities by lowering the percolation threshold of fast 0-TM diffusion channels. Our simulations demonstrate that even a small amount of F substitution can have a strong beneficial effect on the observed capacity, which is especially obvious in the percolation map of **Fig. 5**.

The beneficial effect of fluorination can be explained by the attractive interaction between F and Li atoms in oxyfluoride compositions. As F atoms prefer to be surrounded by Li atoms, the SRO around F atoms results in the formation of Li-rich domains. 0-TM channels, which are diffusion channels that avoid transition metals, are themselves Li rich, and thus, local Li enrichment will increase the concentration of 0-TM channels. Indeed, the concentration of 0-TM channels increases almost linearly with the amount of F substitution, as seen in supporting **Fig. S4**.

The number of 0-TM accessible Li sites also increases with F content (supporting **Fig. S5**); however, the effect is much stronger for compositions with low Li content. As seen in **Fig. S5**, low F contents ($y < 0.05$) do not have a significant effect on the 0-TM connected capacity if the unfluorinated composition is near the percolation threshold ($x = 1.10$ in the figure). A possible reason for this behavior may be that the Li clustering promoted by F substitution counteracts the formation of percolating diffusion pathways.

Note that these trends are based on our simple lattice model that only considers Li–F and M–F interactions. In an actual material, additional SRO arising from cation-cation (Li–M, Li–Li, M–M) interactions might be present that may positively or negatively affect Li transport.[26] For some combinations of transition metals, it is thus possible that small amounts of fluorination might disturb the beneficial SRO that is already present in an unfluorinated material.[26] However, for larger F contents, the beneficial effects of fluorination can be expected to dominate.

The percolation maps in **Figs. 5 and 6** show a temperature dependence; thus, it may be difficult to relate them to real-world materials. However, we can draw a connection to real materials by comparing the *upper critical solution temperature* (UCST)[42] in the one-

dimensional phase diagram for the $LiMO_2$–LiF composition line of **Fig. 4a** with previously reported cluster expansion simulations performed by Richards et al.[38] The UCST, i.e., the maximum of the coexistence line, is approximately $T = 2.5\ J/k_B$ for our lattice model (**Fig. 4a**). The simulations performed by Richards et al. predicted the lowest UCST for $LiFeO_2$ (approximately $T = 2,400$ K) and the highest UCST for $LiCoO_2$ (approximately $T = 3,000$ K). These simulations were based on lattice models that included fitted Li–M interactions, and the simulations did not allow for thermal decomposition or melting, which explains the very high temperatures.

Using the UCST of $LiFeO_2$ as a lower bound, we can roughly relate the relative temperatures in our phase diagrams to an absolute temperature scale using a scaling factor of $1\ J/k_B \approx 960$ K. A temperature of 1,000°C (1,273 K), which is realistic for solid-state synthesis, then corresponds to a scaled temperature of $1.33\ J/k_B$.

The lattice model simulations performed by Richards et al. were themselves only approximate and did not include, for example, free energy contributions from lattice vibrations, likely resulting in an overestimation of the temperature. However, the scaling factor gives us a ballpark number and is in line with our intuition that temperatures above $T = 2\ J/k_B$ are likely not accessible for thermal synthesis.

In the discussion thus far, we have assumed that every Li site that is connected to a percolating 0-TM diffusion pathway contributes to the overall capacity. Owing to the strong Li–F interaction, this picture might change as the fluorine content increases. Previous simulations performed by Kitchaev et al. indicated that Li ions cannot be extracted at feasible voltages when this extraction would give rise to isolated F ions.[27] This effect can lead to trapping of some of the Li atoms within the structure even when their sites are connected to a 0-TM diffusion pathway. In the worst-case scenario that each F atom traps one Li atom, the capacity reduction in our LNF15 compound could amount to 0.15 Li/F.U. However, because each Li atom is coordinated by six anions, a number of which could be F atoms, the actual capacity reduction is much smaller.

V. CONCLUSIONS

We investigated the effect of fluorine substitution on the Li transport in cation-disordered Li-ion battery cathodes using a tailored lattice model for the simulation of SRO caused by

Li−F attraction and M−F repulsion (M = other metal species). Our simulations predict that fluorination has a strong beneficial effect on Li transport and significantly reduces the Li content needed to achieve high capacities. Specifically, the percolation simulations predict that small amounts of Li excess ($\sim 5\%$) are sufficient to achieve high capacities in oxyfluorides, whereas the same compositions would not be percolating for Li without fluorine substitution. We validated this prediction by synthesizing and characterizing new cation-disordered rock-salt compounds with and without fluorine substitution and with only 5% excess Li. The fluorinated compound indeed exhibited superior capacities that were 32–37% greater than those of its unfluorinated counterpart.

Our findings demonstrate that fluorine substitution is generally favorable for Li transport in cation-disordered cathodes and should be considered for materials in which transport becomes performance limiting. The capacity increases proportionally with the fluorine content up to the solubility limit, such that the optimal composition is obtained for maximal thermal fluorination.

VI. ACKNOWLEDGMENTS

This work was supported by Umicore Specialty Oxides and Chemicals and by the Assistant Secretary for Energy Efficiency and Renewable Energy, Vehicle Technologies Office, of the U.S. Department of Energy (DOE) under Contract No. DE-AC02-05CH11231 under the Advanced Battery Materials Research (BMR) Program. This work used the Extreme Science and Engineering Discovery Environment (XSEDE), which is supported by National Science Foundation (NSF) grant no. ACI-1053575, and resources of the National Energy Research Scientific Computing Center (NERSC), a DOE Office of Science User Facility supported by the Office of Science of the DOE under Contract No. DE-C02-05CH11231. Additional computational resources from the University of California Berkeley, HPC Cluster (SAVIO) and from the Lawrencium computational cluster resource provided by the IT Division at the Lawrence Berkeley National Laboratory (Supported by the Director, Office of Science, Office of Basic Energy Sciences, of the DOE under Contract No. DE-AC02-05CH11231) are gratefully acknowledged. ZJ acknowledges financial support from the NSF Graduate Research Fellowship Program (GRFP) under Contract No. DGE 1752814. The authors also thank Huiwen Ji, Penghao Xiao, and Bin Ouyang for fruitful discussions.

Appendix A: Computational and Experimental Details

1. MC Simulations and Percolation Analysis

The GCMC (μVT) phase-diagram calculations were performed using a $4 \times 4 \times 4$ supercell of the primitive rock-salt unit cell containing 128 sites. The Li and F chemical potentials were varied within the ranges $-60 < \mu_{\mathrm{Li}} < 50$ and $-70 < \mu_{\mathrm{F}} < 60$, and a temperature range $0.1 \leq T \leq 8.0\ J/k_{\mathrm{B}}$ was sampled. These settings resulted in ∼2,800,000 $(\mu_{\mathrm{Li}}, \mu_{\mathrm{F}}, T)$ combinations, out of which ∼764,000 fell into the relevant composition space and were considered for the construction of the phase diagram in **Fig. 3**.

For convergence of the percolation properties with good accuracy, the canonical MC simulations were performed using a larger $12 \times 10 \times 10$ rock-salt supercell containing a total of 2,400 sites. Each MC step consisted of N Metropolis attempts to interchange the species of two randomly picked sites, where $N = 2,400$ is the total number of sites in the structure. For each sampled composition and temperature, 200 MC steps were run for equilibration, which was followed by 10,000 production MC steps. The structures after each 20 MC steps were stored for analysis, resulting in a total of 500 configurations per composition over which the percolation properties were averaged.

2. First-Principles Diffusion Path Calculations

All the density functional theory (DFT) calculations used the Perdew-Burke-Ernzerhof[43,44] exchange-correlation functional and projector-augmented wave pseudopotentials,[45] as implemented in the Vienna Ab-Initio Simulation Package (VASP).[46,47] A plane-wave energy cutoff of 520 eV was employed, and gamma-centered k-point meshes with $\lceil 25\,|\vec{b}_i| \rceil$ k-points in each reciprocal lattice direction i were used, where $\vec{b}_i$ is the ith reciprocal lattice vector. Diffusion path calculations were performed using the climbing-image (CI) nudged elastic band (NEB) method[36,37] with five intermediate images. The NEB calculations were performed for di-vacancy diffusion in a quasi-random structure (SQS)[34] model with composition $LiTiO_2$ ($Li_{16}Ti_{16}O_{32}$ and supercells thereof) that was originally constructed by Shin et al. for the simulation of close-packed alloys.[35]

3. Synthesis and Characterization

$Li_{1.05}Ni_{0.458}Ti_{0.458}Mo_{0.033}O_2$ (LNO) and $Li_{1.05}Ni_{0.533}Ti_{0.373}Mo_{0.033}O_{1.85}F_{0.15}$ (LNF15) were synthesized using a traditional solid-state method. Li_2CO_3 (Alfa Aesar, ACS, 99% min), $NiCO_3$ (Alfa Aesar, 98%), TiO_2 (Anatase, Alfa Aesar, 99.9%), MoO_2 (Alfa Aesar, 99%), and LiF (Alfa Aesar, 99.99%) were used as precursors. All the precursors were stoichiometrically mixed (except for adding 5% more Li_2CO_3 and 4% more $NiCO_3$ to compensate for possible loss during synthesis[19,40]) with a Retsch PM 200 planetary ball mill at a rate of 300 rpm for 4 h. The precursors were then pelletized and sintered at 750°C in air for 3 h, followed by quenching in air. The pellets were then transferred to a glovebox and ground into powders.

To prepare the cathode films, composed of active materials, SUPER C65 (Timcal), and polytetrafluoroethylene (PTFE, DuPont, Teflon 8A) at a weight ratio of 70:20:10, 280 mg of active materials and 80 mg of SUPER C65 were mixed and shaker-milled for 20 min in an argon atmosphere with a SPEX 800M Mixer/Mill, and PTFE was later added and manually mixed with the shaker-milled mixture for 40 min. The components were then rolled into thin films inside the glovebox. Commercialized 1 M LiPF6 in ethylene carbonate (EC) and dimethyl carbonate (DMC) solution (volume ratio 1:1) was used as the electrolyte. Glass microfibers (Whatman) were used as the separator, and FMC Li metal foil was used as the anode. Coin cells were assembled inside the glovebox and tested on an Arbin battery tester at room temperature. The loading density of the films was approximately 5 $mg\,cm^{-2}$ based on the weight of the active materials. The specific capacities were then calculated based on the weight of the active materials (70%) in the cathode films.

X-ray diffraction (XRD) patterns of the as-synthesized compounds were obtained using a Bruker D8 Advance A25 diffractometer (Cu source) in the 2θ range of 20°–85°. Rietveld refinement was performed using PANalytical X'pert HighScore Plus software.

REFERENCES

[1]J. Lee, A. Urban, X. Li, D. Su, G. Hautier, and G. Ceder, Science **343**, 519 (2014).

[2]N. Yabuuchi, Chem. Rec. (2018), 10.1002/tcr.201800089.

[3]N. Yabuuchi, M. Takeuchi, M. Nakayama, H. Shiiba, M. Ogawa, K. Nakayama, T. Ohta, D. Endo, T. Ozaki, T. Inamasu, K. Sato, and S. Komaba, Proc. Natl. Acad. Sci. USA **112**, 7650–7655 (2015).

[4]R. Chen, S. Ren, M. Knapp, D. Wang, R. Witter, M. Fichtner, and H. Hahn, Adv. Energy Mater. **5**, 1401814 (2015).

[5]R. Chen, R. Witte, R. Heinzmann, S. Ren, S. Mangold, H. Hahn, R. Hempelmann, H. Ehrenberg, and S. Indris, Phys. Chem. Chem. Phys. **18**, 7695 (2016).

[6]N. Yabuuchi, Y. Tahara, S. Komaba, S. Kitada, and Y. Kajiya, Chem. Mater. **28**, 416 (2016).

[7]N. Yabuuchi, M. Takeuchi, S. Komaba, S. Ichikawa, T. Ozaki, and T. Inamasu, Chem. Commun. **52**, 2051 (2016).

[8]A. Urban, A. Abdellahi, S. Dacek, N. Artrith, and G. Ceder, Phys. Rev. Lett. **119**, 176402 (2017).

[9]S. Hoshino, A. M. Glushenkov, S. Ichikawa, T. Ozaki, T. Inamasu, and N. Yabuuchi, ACS Energy Lett. **2**, 733 (2017).

[10]P. Rozier, E. Iwama, N. Nishio, K. Baba, K. Matsumura, K. Kisu, J. Miyamoto, W. Naoi, Y. Orikasa, P. Simon, and K. Naoi, Chem. Mater. **30**, 4926 (2018).

[11]J. Lee, D. A. Kitchaev, D.-H. Kwon, C.-W. Lee, J. K. Papp, Y.-S. Liu, Z. Lun, R. J. Clément, T. Shi, B. D. McCloskey, J. Guo, M. Balasubramanian, and G. Ceder, Nature **556**, 185 (2018).

[12]A. Urban, J. Lee, and G. Ceder, Adv. Energy Mater. **4**, 1400478 (2014).

[13]A. R. Naghash and J. Y. Lee, Electrochim. Acta **46**, 2293 (2001).

[14]I. D. Gocheva, I. Tanaka, T. Doi, S. Okada, and Y. Jun-ichi, Electrochem. Commun. **11**, 1583 (2009).

[15]N. Pereira, F. Badway, M. Wartelsky, S. Gunn, and G. G. Amatucci, J. Electrochem. Soc. **156**, A407 (2009).

[16]W. Tong, W.-S. Yoon, N. M. Hagh, and G. G. Amatucci, Chem. Mater. **21**, 2139 (2009).

[17]W. Choi and A. Manthiram, Electrochem. Solid-State Lett. **9**, A245 (2006).

[18]A. Windmüller, C. A. Bridges, C.-L. Tsai, S. Lobe, C. Dellen, G. M. Veith, M. Finsterbusch, S. Uhlenbruck, and O. Guillon, ACS Appl. Energy Mater. **1**, 715 (2018).

[19]J. Lee, J. K. Papp, R. J. Clément, S. Sallis, D.-H. Kwon, T. Shi, W. Yang, B. D. McCloskey, and G. Ceder, Nat. Commun. **8**, 981 (2017).

[20]Z. Lun, B. Ouyang, D. A. Kitchaev, R. J. Clément, J. K. Papp, M. Balasubramanian, Y. Tian, T. Lei, T. Shi, B. D. McCloskey, J. Lee, and G. Ceder, Adv. Energy Mater. , 1802959 (2018).

[21]R. Chen, S. Ren, M. Yavuz, A. A. Guda, V. Shapovalov, R. Witter, M. Fichtner, and H. Hahn, Phys. Chem. Chem. Phys. **17**, 17288–17295 (2015).

[22]S. Ren, R. Chen, E. Maawad, O. Dolotko, A. A. Guda, V. Shapovalov, D. Wang, H. Hahn, and M. Fichtner, Adv. Sci. **2**, 1500128 (2015).

[23]N. Takeda, S. Hoshino, L. Xie, S. Chen, I. Ikeuchi, R. Natsui, K. Nakura, and N. Yabuuchi, J. Power Sources **367**, 122 (2017).

[24]X. Wang, Y. Huang, D. Ji, F. Omenya, K. Karki, S. Sallis, L. F. J. Piper, K. M. Wiaderek, K. W. Chapman, N. A. Chernova, and M. S. Whittingham, J. Electrochem. Soc. **164**, A1552 (2017).

[25]R. A. House, L. Jin, U. Maitra, K. Tsuruta, J. W. Somerville, D. P. Förstermann, F. Massel, L. Duda, M. R. Roberts, and P. G. Bruce, Energy Environ. Sci. **11**, 926 (2018).

[26]H. Ji, A. Urban, D. A. Kitchaev, D.-H. Kwon, N. Artrith, C. Ophus, W. Huang, Z. Cai, T. Shi, J. C. Kim, and G. Ceder, arXiv , 1806.06096 (2018).

[27]D. A. Kitchaev, Z. Lun, W. D. Richards, H. Ji, R. J. Clément, M. Balasubramanian, D.-H. Kwon, K. Dai, J. K. Papp, T. Lei, B. D. McCloskey, W. Yang, J. Lee, and G. Ceder, Energy Environ. Sci. **11**, 2159 (2018).

[28]R. J. Clément, D. Kitchaev, J. Lee, and G. Ceder, Chem. Mater. **30**, 6945 (2018).

[29]A. Van der Ven and G. Ceder, Electrochem. Solid-State Lett. **3**, 301 (2000).

[30]A. Van der Ven, J. Bhattacharya, and A. A. Belak, Acc. Chem. Res. **46**, 1216 (2013).

[31]K. Kang and G. Ceder, Phys. Rev. B **74**, 094105 (2006).

[32]N. Artrith, G. Ceder, and A. Urban, to be published (2019).

[33]D. Landau and K. Binder, *Monte Carlo Simulations in Statistical Physics* (Cambridge University Press, 2009).

[34]A. Zunger, S.-H. Wei, L. G. Ferreira, and J. E. Bernard, Phys. Rev. Lett. **65**, 353 (1990).

[35]D. Shin, A. van de Walle, Y. Wang, and Z.-K. Liu, Phys. Rev. B **76**, 144204 (2007).

[36]H. Jónsson, G. Mills, and K. W. Jacobsen, "Classical and quantum dynamics in condensed phase simulations," (World Scientific, 1998) Chap. Nudged Elastic Band Method for Finding Minimum Energy Paths of Transitions, pp. 385–404.

[37]G. Henkelman, B. Uberuaga, and H. Jónsson, J. Chem. Phys. **113**, 9901 (2000).

[38]W. D. Richards, S. T. Dacek, D. A. Kitchaev, and G. Ceder, Adv. Energy Mater. **8**, 1701533 (2017).

[39]L. Zhang, H. Noguchi, D. Li, T. Muta, X. Wang, M. Yoshio, and I. Taniguchi, J. Power Sources **185**, 534–541 (2008).

[40]J. Lee, D.-H. Seo, M. Balasubramanian, N. Twu, X. Li, and G. Ceder, Energy Environ. Sci. **8**, 3255–3265 (2015).

[41]N. Nitta, F. Wu, J. T. Lee, and G. Yushin, Mater. Today **18**, 252 (2015).

[42]D. A. Porter and K. E. Easterling, *Phase Transformations in Metals and Alloys* (Springer, 1992).

[43]J. Perdew, K. Burke, and M. Ernzerhof, Phys. Rev. Lett. **77**, 3865 (1996).

[44]J. P. Perdew, K. Burke, and M. Ernzerhof, Phys. Rev. Lett. **78**, 1396 (1997).

[45]P. E. Blöchl, Phys. Rev. B **50**, 17953 (1994).

[46]G. Kresse and J. Furthmüller, Comput. Mater. Sci. **6**, 15 (1996).

[47]G. Kresse and J. Furthmüller, Phys. Rev. B **54**, 11169 (1996).

SI: Version 2.1 (draft) as of 2018-11-27
Primary author: N. Artrith

Supporting Information:
Effect of Fluorination on Lithium Transport in Rock-Salt-Type Lithium-Ion Battery Cathodes

Nongnuch Artrith,[1,2,a)] Zhengyan Lun,[1,2] Zinab Jadidi,[1,2] Alexander Urban,[3] and Gerbrand Ceder[1,2,b)]

[1)] *Department of Materials Science and Engineering, University of California, Berkeley, CA, USA*

[2)] *Materials Science Division, Lawrence Berkeley National Laboratory, Berkeley, CA, USA*

[3)] *School of Chemistry, University of St Andrews, UK*

(Dated: 2018-11-27)

[a)]Electronic mail: nartrith@atomistic.net

[b)]Electronic mail: gceder@berkeley.edu

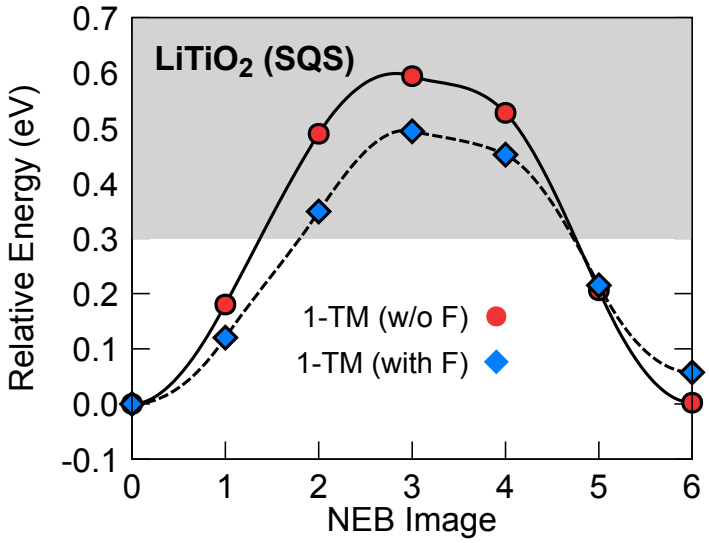

FIG. S1. **Impact of fluorination on a 1-TM channel.** The plot shows the minimum energy paths (MEPs) obtained from nudged-elastic band (NEB) calculations for a 1-TM channel in an unfluorinated (red circles) and in a fluorinated (blue diamonds) special quasi-random structure (SQS) with composition $LiTiO_2$ ($Li_{16}Ti_{16}O_{32}$). In the fluorinated structure, one of the four oxygen atoms around the 1-TM channel was replaced by a fluorine atom. For both diffusion paths a second vacancy was created so that the diffusion could occur via the divacancy mechanism. In Li-ion battery cathodes, diffusion channels with activation barriers greater than 0.3 eV are typically considered inactive,[1,2] and this threshold is indicated by the gray region in the figure. Fluorine substitution does slightly change the diffusion barrier from around 0.6 eV to around 0.5 eV, but the effect is not large enough to activate the 1-TM channel.

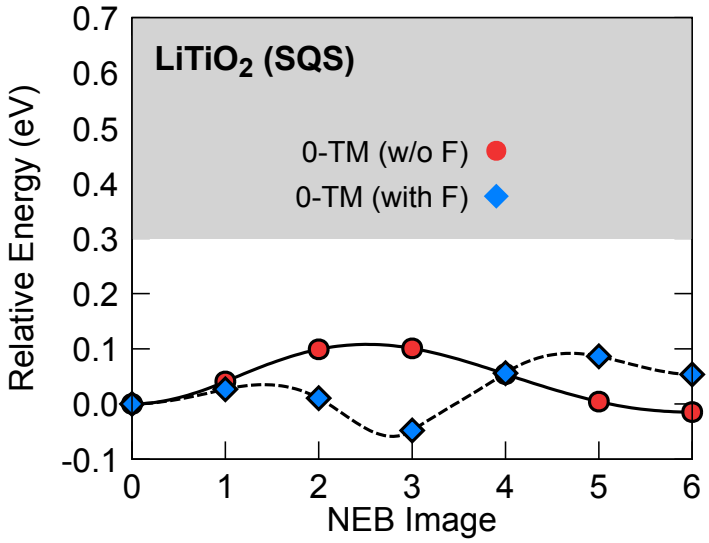

FIG. S2. **Impact of fluorination on a 0-TM channel.** The plot shows the MEPs obtained from NEB calculations for a 0-TM channel in an unfluorinated (red circles) and in a fluorinated (blue diamonds) SQS with composition $LiTiO_2$ ($Li_{16}Ti_{16}O_{32}$). As in the case of the 1-TM channel in Fig. S1, in the fluorinated structure, one of the four oxygen atoms around the 0-TM channel was replaced by a fluorine atom, and the divacancy mechanism was considered. Again, fluorination changes the MEP slightly, but the overall diffusion barrier is not significantly affected and the 0-TM channel remains active. Note that the tetrahedral site (NEB image 3) is stabilized in the fluorinated structure. However, this does not alter the overall diffusion pathway and is of no consequence for the percolation analysis.

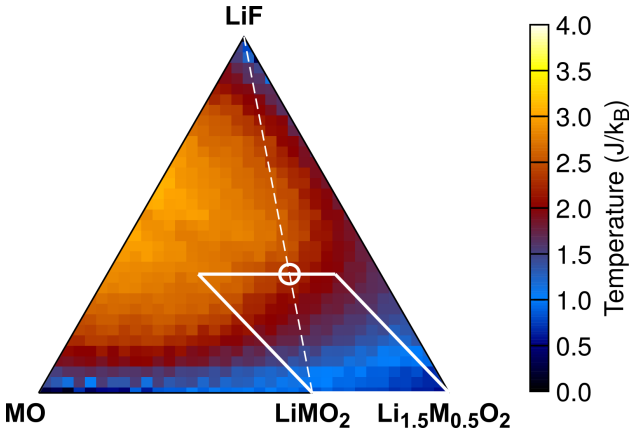

FIG. S3. **Gibbs-triangle representation of the phase diagram of Fig. 3a in the main text.** The colors are according to the legend in Fig. 3a and encode the lowest temperature at which a composition is observed in the grand-canonical Monte-Carlo (GCMC) simulations. The region enclosed by the solid white rhomboid corresponds to that shown in Fig. 3b in the main text. The white circle indicates the Li_2MO_2F composition. The GCMC phase-diagram calculations were done using a $4 \times 4 \times 4$ supercell of the primitive rock-salt unit cell containing 128 sites.

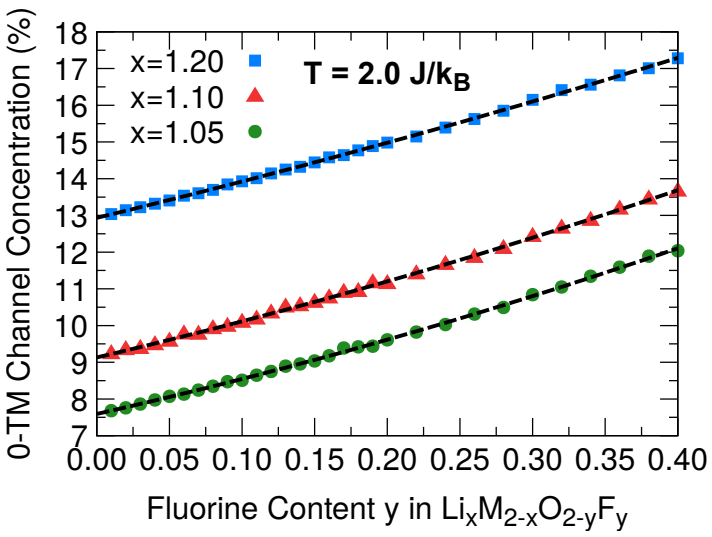

FIG. S4. **Increase of the 0-TM channel concentration with fluorination.** The figure shows the change of the concentration of 0-TM channels relative to all tetrahedral cation clusters as function of the fluorine content as obtained from canonical MC simulations. The 0-TM channel concentration is $c_{0\text{-TM}} = N_{0\text{-TM}}/(N_{0\text{-TM}} + N_{1\text{-TM}} + N_{2\text{-TM}} + N_{3\text{-TM}} + N_{4\text{-TM}})$ where $N_{n\text{-TM}}$ is the total number of n-TM clusters in the structure. Three different Li contents are shown: $x = 1.05$ (green circles), $x = 1.10$ (red triangles), and $x = 1.20$ (blue squares) with the overall composition $\mathrm{Li}_x\mathrm{M}_{2-x}\mathrm{O}_{2-y}\mathrm{F}_y$. As seen in the figure, independent of the Li content, the 0-TM channel concentration increases almost linearly with the fluorine content. The figure shows data for a temperature of $J = 2.0\ J/k_{\mathrm{B}}$. For lower temperatures the trend is the same but the slope is steeper (not shown). The canonical MC simulations were performed using a $12 \times 10 \times 10$ rock-salt supercell containing a total of 2,400 sites.

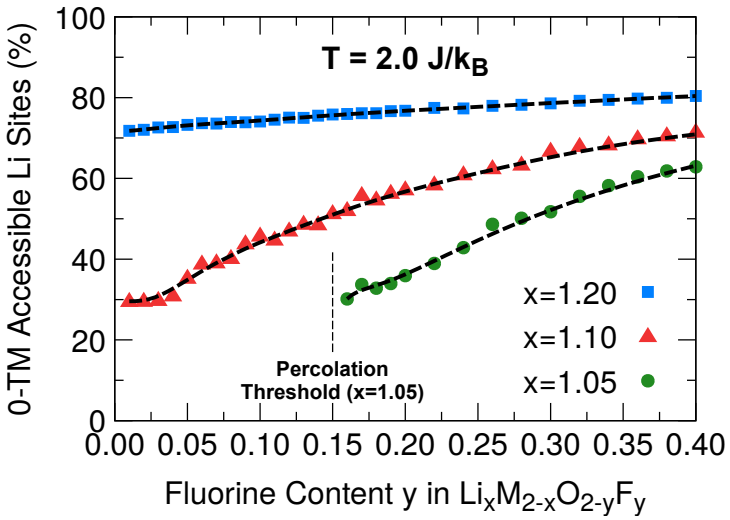

FIG. S5. **Change of the 0-TM connected capacity with fluorination.** Unlike the 0-TM channel concentration shown in Fig. S4, the 0-TM connected capacity (in terms of the 0-TM accessible Li sites) does not increase in the same way for each Li content. The effect of fluorination is strong for low Li contents ($x = 1.05$ and $x = 1.10$), and is small for $x = 1.20$. The capacity does not increase linearly, and in the case of $x = 1.10$ F substitution of less than $y = 0.05$ (2.5%) has no significant effect. The canonical MC simulations were performed using a $12 \times 10 \times 10$ rock-salt supercell containing a total of 2,400 sites.

REFERENCES

[1]K. Kang and G. Ceder, Phys. Rev. B **74**, 094105 (2006).

[2]J. Lee, A. Urban, X. Li, D. Su, G. Hautier, and G. Ceder, Science **343**, 519 (2014).